ADVANCED FUNCTIONAL MATERIALS
www.afm-journal.de

Immobilization of Quantum Dots in Nanostructured Porous Silicon Films: Characterizations and Signal Amplification for Dual-Mode Optical Biosensing

Girija Gaur, Dmitry S. Koktysh, and Sharon M. Weiss**

Highly sensitive dual-mode labeled detection of biotin in well-characterized porous silicon (PSi) films using colloidal quantum dots (QDs) as signal amplifiers are demonstrated. Optimization of the PSi platform for targeted QD infiltration and immobilization is carried out by characterizing and tuning the porosity, film depth, and pore size. Binding events of target QD-biotin conjugates with streptavidin probes immobilized on the pore walls are monitored by reflective interferometric spectroscopy and fluorescence measurements. QD labeling of the target biotin molecules enables detection based on a distinct fluorescent signal as well as a greater than 5-fold enhancement in the measured spectral reflectance fringe shift and a nearly three order of magnitude improvement in the detection limit for only 6% surface area coverage of QDs inside the porous matrix. Utilizing the QD signal amplifiers, an exceptional biotin detection limit of ≈6 fg mm^{-2} is demonstrated with sub-fg mm^{-2} detection limits achievable.

1. Introduction

In recent years, biocompatible luminescent colloidal quantum dots (QDs) have gained increasing attention for numerous biomedical applications such as fluorescent tags in biomarkers, immunoassays, guided drug delivery, cellular imaging, and fluorescence resonance energy transfer (FRET) based sensors.[1–6] The unique photophysical properties of QDs, including high quantum yield, resistance to photobleaching, broad excitation spectra, tunable by nanometer size and structure, fluorescence that spans the UV-visible-NIR spectrum and bioconjugation capabilities make them a favorable choice for meeting the increasing demands of high sensitivity, stability, and rapid signal transduction in the early detection of toxins, disease markers, chemical species, and environmental bio-agents.[7–12] However, most QD-labeled sensing platforms to date have focused on using the strong fluorescence spectra of protein- or DNA-conjugated QDs for target molecule detection via fluorescence immunoassays or FRET.[13–16] Although FRET based biosensing has demonstrated sensitivities down to the single molecule, the method is hindered by the extreme sensitivity to distance between donor and acceptor molecules and the requirement for spectral overlap between donor emission and acceptor absorption for efficient energy transfer.[17–19] The conveniently high refractive index of QDs compared to that of conjugated protein or DNA molecules is a potential advantage for sensor platforms that has been left largely unexploited. In this work, we utilize the simplicity of fluorescence based optical detection of QD-conjugated biomolecules and combine it with the ability to quantify captured target molecules in thin films via monitoring changes in the effective refractive index of the film by reflective interferometric spectroscopy to achieve a novel, dual-mode, optical porous silicon (PSi) sensor.

Our choice for selecting PSi as the material in which to incorporate QD-labeled biomolecules stems from the many advantages that PSi has to offer as a sensor platform, such as tunable pore dimensions and film thicknesses, high surface area (>100 m^2 cm^{-3}), ease of surface modification, and inherent size-selective filtering of contaminant molecules.[20–24] These advantages have led to the emergence of many PSi based label-free biosensors,[25–27] as well as the implementation of PSi films and membranes in fuel cells,[28–30] solar cells,[31–33] drug delivery vehicles,[34–38] and cellular imaging host matrices.[39–41] For all of these applications, PSi pore size distributions, pore morphologies, available surface area for binding events to take place, and stable surface functionalization procedures play a crucial role. A comprehensive step-by-step characterization of the PSi platform has therefore been undertaken in this work using reflectance spectroscopy, Fourier transform infrared spectroscopy (FTIR), and scanning electron microscopy (SEM) to more accurately enable estimation of infiltration efficiency, quantification of captured molecules in the nanoporous matrix, and optimization of the PSi sensor for maximum signal trans-

G. Gaur, Prof. S. M. Weiss
Department of Electrical Engineering
and Computer Science,
Vanderbilt University
Nashville, TN 37235, USA
E-mail: sharon.weiss@vanderbilt.edu
Prof. D. S. Koktysh
Department of Chemistry
Vanderbilt Institute of Nanoscale Science and Engineering
Nashville, TN 37235, USA
E-mail: dmitry.koktysh@vanderbilt.edu

DOI: 10.1002/adfm.201202697

duction depending upon the size of target infiltrated species. With a well-characterized and appropriately functionalized PSi matrix, we demonstrate the specific detection of biotin molecules conjugated with low-toxicity $AgInS_2$/ZnS (AIS/ZnS) QDs through both reflectance and fluorescence measurements. The QDs serve both as high refractive index signal amplifiers for the reflectance measurements that can quantify the number of molecules captured and as fluorescent emitters whose characteristic emission wavelength confirms molecule capture in the functionalized pores. We note that intermediate QD carrier nanoparticles and additional biomolecule labeling are not necessary using our approach.[42] Moreover, an extremely competitive detection sensitivity of 6 fg mm^{-2} for biotin molecules is shown and we anticipate that a sub-fg mm^{-2} detection limit is readily achievable.

2. Porous Silicon Characterization

PSi films were fabricated using a standard electrochemical etching technique. The morphology of PSi depends not only on the etching parameters used during fabrication but also on silicon wafer characteristics such as type of dopant, resistivity, and orientation. In order to accurately model the properties of the PSi films, top-view and cross-sectional scanning electron microscopy (SEM) images were analyzed to determine pore size distributions, number of pores, and the available surface area for molecular binding events. Knowledge of the pore size distribution in a given film is essential for sensing applications in order to understand the balance between efficient infiltration of target molecules and natural filtering of large contaminant species whose presence in the pores might lead to false positive sensor readings. Knowledge of the number of pores and associated surface area available for molecular binding inside the pores is critical for understanding how many molecules can be captured by PSi sensors,[24] leading to measurable signals and enhancements in sensitivity for small molecule detection.

For our initial characterization study, several PSi films of the same nominal thickness were formed under different applied current densities to understand the range of achievable pore sizes, porosities, and morphologies. The etching parameters for these ≈5.5 μm thick PSi films are presented in **Table 1**. Porosity calculations were based on gravimetric analysis of the PSi layers. **Figure 1** shows top-view SEM images with the corresponding pore size histograms derived from SEM image analysis. Based on the results shown in Figure 1 and the corresponding fabrication conditions in Table 1, we find that increasing the etching current density results in larger pore sizes with cylindrical pore geometries, higher porosities, fewer side branches, and a slightly broader pore size distribution (see Supporting Information Figure S1). These trends agree well with previously reported results.[43,44]

Table 1. Fabrication conditions for ≈5.5 μm thick PSi films with different average pore sizes.

Average Pore Diameter [nm]	% Porosity (± 2.5%)	Etching Current Density [mA cm^{-2}]	Etching Time [s]
30	82	60	190
25	75	48	200
20	67	40	210
15	60	20	510
12	55	5	1200

Figure 2 shows quantification of the decrease in PSi surface area that accompanies increasing average pore diameters and increasing porosity. For the surface area calculations, pores have been assumed to be cylindrical. This approach underestimates the total surface area in the porous matrix as it neglects the surface area contribution from the side branches. Nitrogen adsorption measurements conducted for the films with average pore diameters of 25 nm suggest a surface area of 260 cm^2 for 1 μm depth in the PSi film, which is approximately 10% greater than the 230 cm^2 per 1 μm depth estimated from top-view SEM images of the PSi film in which side-wall branches and surface irregularities have been neglected. For biomolecule immobilization in the PSi framework, these sidewall branches (1 nm – 5 nm in diameter) are inaccessible and can be neglected for target analyte surface area coverage estimations. The surface area on all samples examined was ≥100 m^2 cm^{-3}, which represents a very large active sensing region for molecular detection. There is a natural tradeoff between available surface area for molecular attachment and ease of infiltrating molecules into larger and more open porous frameworks. We note that the surface functionalization procedures for sensing applications must be carefully tuned to allow for high target molecule capture relative to the available surface area. For example, a sufficient number of probe molecules must be immobilized in the pores to ensure that target molecule capture leads to a measurable sensor output.

3. Characterization of PSi Surface Functionalization for QD Immobilization and Dual-Mode Biosensing Studies

PSi films were functionalized in order to allow the specific attachment of desired molecules. In our studies to evaluate the infiltration efficiency of various sized species in PSi films of different thicknesses with the pore size distributions shown in Figure 1, an amine termination was needed. **Figure 3**a shows the FTIR spectra for a PSi film after anodization, thermal oxidation, and silanization with 3-aminopropyltriethoxysilane to form the amine termination. For the as-anodized film, resonances near 2105 cm^{-1} and 2115 cm^{-1}, corresponding to SiH_x bonds, confirm the expected hydride termination. After thermal treatment, the PSi film exhibits absorption resonances near 1040 cm^{-1} and 1140 cm^{-1}, indicating the presence of Si–O–Si bonding and confirming oxidation of the PSi film. Silanization of the oxidized PSi film results in several distinct features appearing in the FTIR spectrum that demonstrate the presence of amino groups on the surface. The broader resonances near 3300 cm^{-1} represent NH_2 stretch vibrations while the two resonances at 2880 cm^{-1} and 2940 cm^{-1} specify the -C-NH_2 stretch vibration. Moreover, siloxane bond formations between silane and the hydroxyl terminated groups on oxidized PSi are seen between the region 1300 cm^{-1} and 1730 cm^{-1} with small peaks near 1407 cm^{-1}, 1508 cm^{-1}, 1575 cm^{-1} and 1650 cm^{-1} corresponding to the CH_3 group of APTES, symmetric $-NH^{3+}$

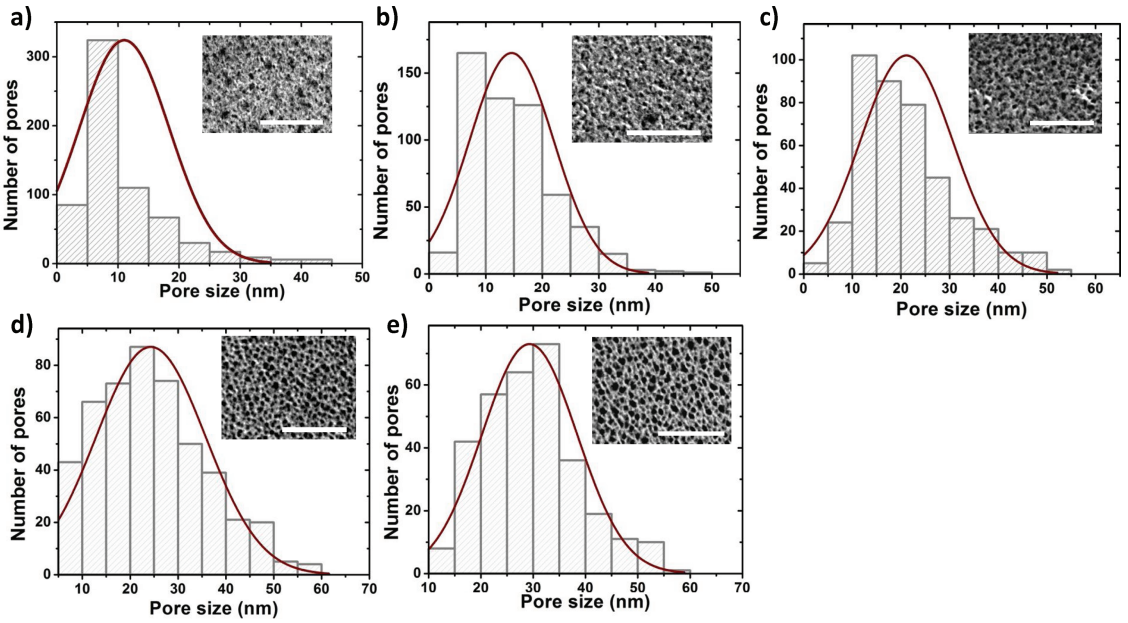

Figure 1. Top-view SEM images of PSi films and the corresponding pore size distributions. The etching conditions for these films are given in Table 1. a) 12 nm average pore size ($\sigma = 7.87$ nm), b) 15 nm average pore size ($\sigma = 6$ nm), c) 20 nm average pore size ($\sigma = 10.35$ nm), d) 25 nm average pore size ($\sigma = 11.21$ nm), and e) 30 nm average pore size ($\sigma = 9.78$ nm). All scale bars indicate 375 nm.

deformation mode, NH_2 scissoring vibration mode, and the asymmetric $-NH^{3+}$ deformation mode, respectively.[45] For the sensing studies of the biotin-streptavidin pair (Section 4), additional functionalization steps were required and the associated FTIR spectra are shown in Figure 3b. Glutaraldehyde binding with silane can be confirmed from the resonances at 1650 cm^{-1} and 1872 cm^{-1} (not shown) due to C=O stretching of the aldehyde group and at 1465 cm^{-1} arising from the C=O vibration mode. A more distinct peak formation at 2940 cm^{-1} can be attributed to the C-H stretching modes from glutaraldehyde functionalization. Peaks representing amide bonds of streptavidin are detected near 1529 cm^{-1} and 1670 cm^{-1}. A very broad peak in the region between 3100 cm^{-1} and 3600 cm^{-1} indicates the presence of exchangeable protons from the amide peptide groups of streptavidin and due to the O-H and N-H stretching modes of glutaraldehyde and streptavidin.

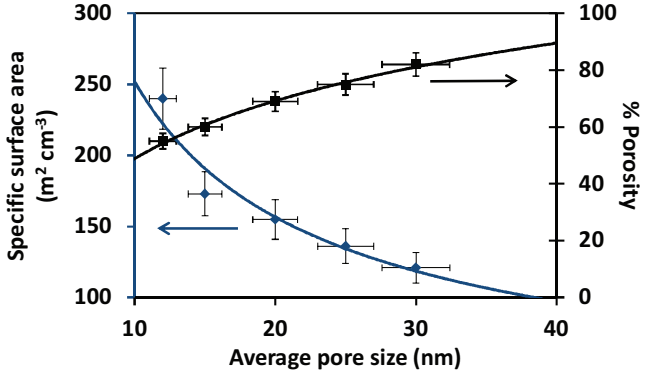

Figure 2. Inverse relationship between PSi surface area and porosity as a function of average pore size. The solid lines serve as guides to the eye.

4. QD infiltration and Binding in PSi Films

4.1. Dependence of PSi-QD Coupling on PSi film Thickness

Studies were conducted to explore the infiltration efficiency of QDs into PSi films in order to verify that QD-labeled biosening in nanoscale pores is feasible. First, the dependence of PSi-QD coupling on PSi film thickness was evaluated by studying the uniformity of QD surface coverages on the pore walls and to determine how deeply QDs infiltrate into PSi films. Next, the influence of the pore size on QD infiltration efficiency was explored (Section 4.2). PbS QDs, 2.8 nm in size, were selected for these initial studies.

In order to investigate the uniformity of QD surface coverage in PSi films, two sets of amine-functionalized PSi layers of 2 μm, 3.75 μm, 5.5 μm and 7.25 μm thickness were fabricated: one set had an average pore size of 12 nm and the other 25 nm. The amine-functionalization on the PSi films ensured that a monolayer of PbS QDs could be attached to the pore walls. Reflectance spectra were collected during the surface functionalization procedure and after coupling the colloidal PbS QDs to the PSi films to probe changes in the effective refractive index of the films due to QD infiltration. The relative change in effective index due to QD infiltration should remain constant across different PSi film thicknesses if the QDs infiltrate uniformly throughout the films. **Figure 4**a shows a schematic illustration of a PSi film before and after QD infiltration and the associated reflectance spectra Figure 4b for one of the films in the study. The red shift of the reflectance spectra suggests that both amine linker molecules and the small QDs are successfully added to the PSi film. In order to provide a direct way of quantifying the effective refractive index of the different

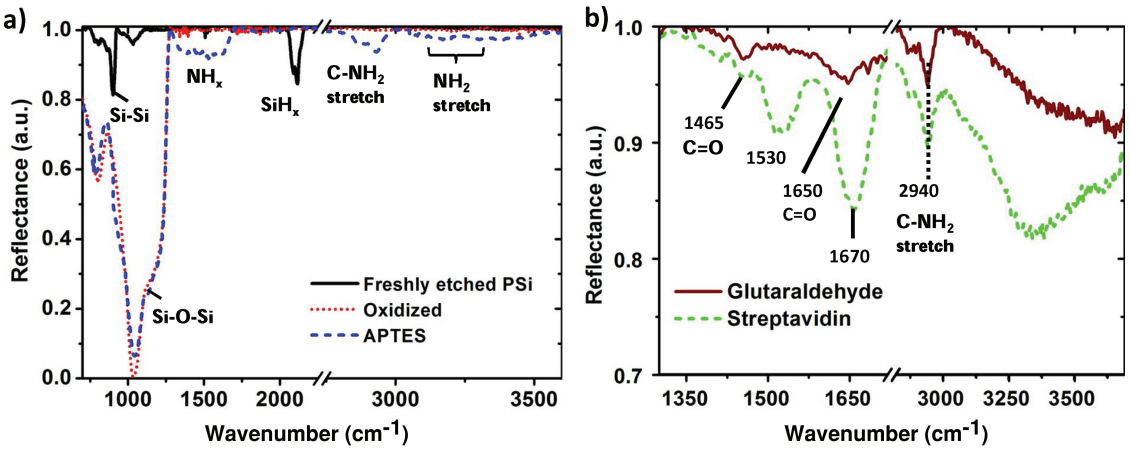

Figure 3. a) FTIR measurements in reflectance mode of a freshly anodized PSi sample that subsequently undergoes thermal oxidation and APTES surface modification. b) FTIR spectra of same sample after attachment of glutaraldehyde and streptavidin for QD-biotin conjugate detection in PSi.

PSi layers and the associated changes in effective optical thickness (EOT) of the films upon inclusion of APTES and QDs, fast Fourier transform (FFT) analysis of the collected white light reflectance spectra was performed.[20,46] The Fabry-Perot relationship for thin film interference states that the reflectance fringe maxima are described by the relationship given by Equation (1).

$$m\lambda = 2nL \quad (1)$$

Here λ is the wavelength of incident light, n is the refractive index of the material, L is the film thickness, and m is an integer. Taking a FFT of the reflectance data as a function of wave number using a Hamming window produces a peak corresponding to the term $2nL$, which is the EOT of the PSi layer.[20]

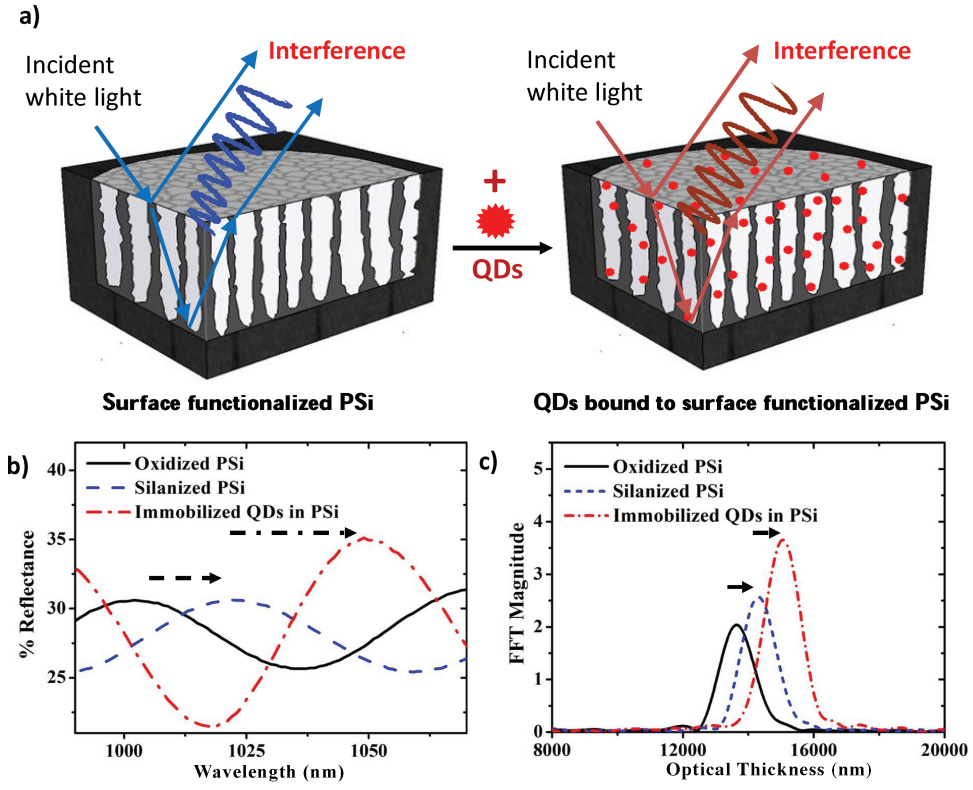

Figure 4. a) Schematic representation of surface functionalized PSi film before and after attachment of QDs. Light reflecting off the top and bottom interfaces of the film interfere and produce characteristic Fabry-Perot fringes. b) Reflectance fringe shifts and c) increase in EOT for an oxidized ≈5.5 µm thick PSi layer with 20 nm average pore diameter after APTES surface functionalization and immobilizing 2.8 nm PbS QDs. The increase in spectral shift and FFT amplitude demonstrate that QDs are being covalently bound to the functionalized pore walls.

Table 2. Relative increase in optical thickness of PSi films after coupling with 2.8 nm QDs. All data points represent the average of measurements from at least two different samples.

Layer Thickness [μm]	Relative increase in optical thickness of PSi layer $\Delta nL/(nL_0)$	
	25 nm pores	10 nm pores
2.00	0.042 ± 4.1%	0.024 ± 5%
3.75	0.043 ± 3%	0.023 ± 4.4%
5.50	0.043 ± 3.2%	0.025 ± 4%
7.25	0.040 ± 3.1%	0.024 ± 4.2%

Figure 4c shows the EOT data corresponding to the reflectance data collected over the wavelength range of 500 nm to 2000 nm (Supporting Information Figure S2).

The magnitude of the FFT peaks corresponds to the ratio of effective refractive index contrast at each layer interface. With the addition of material to the porous matrix, the effective refractive index of the PSi layer increases; accordingly, the FFT peak height increases along with the EOT after each infiltration step in the study.

The relative EOT increase of all PSi films examined in this study after QD coupling is shown in **Table 2**. The uniform relative increase in EOT for all the PSi films with a given pore size suggests that 2.8 nm PbS QDs can effectively infiltrate PSi films with diameters equal to or greater than 12 nm to at least a thickness of 7.25 μm with a uniform surface density distribution. The surface density of the QDs, however, is different for PSi films with different pore diameters, as is further explored in Section 4.2. Note that the uniform relative increase in EOT for films with the same average pore diameter corresponds to an almost linear increase in the PSi effective refractive index with increasing layer thickness. The uniform infiltration and attachment of QDs in the porous matrix demonstrates that sensors based on PSi films can utilize the entire accessible surface area of the porous matrix without being limited to probing only the sensor top surface. We note that energy dispersive X-ray spectroscopy was also performed (Supporting Information Figure S3) to further verify that the PbS QDs are bound inside the pores of the films. The elemental presence of lead and sulfur within the porous matrix was confirmed. This result agrees well with previously reported research in which SEM images showed that 7.5 nm PbS QDs were uniformly coupled with the pore walls of a PSi film with 70 nm pores.[47]

4.2. Dependence of PSi-QD Coupling on PSi Pore Size to Target QD Size Ratio

The influence of target–pore size ratio on the efficiency of infiltrating QDs into the PSi films has been studied by infiltrating two different sized PbS QDs (≈2.8 nm and ≈7.5 nm, as shown in **Figure 5**) into 5.5 μm thick PSi films with five different average pore diameters (12, 15, 20, 25, and 30 nm).

In general, the ease of infiltrating species into a nanoporous framework increases with increasing pore sizes. However, as shown in Figure 2, the available specific surface area for immobilizing species inside the porous matrix decreases with an increase in pore size, which limits the number of available binding sites. In order to maximize detection sensitivity for sensors based on porous materials, the trade-off between the pore size to target QD size ratio and the specific surface area needs to be balanced such that pore sizes are large enough to allow for infiltration of targeted biological or chemical species into the porous matrix while providing the maximum possible specific surface area for immobilization.

Transfer matrix simulations[48] were performed to estimate the number of surface bound QDs and the percent surface area coverage of the QDs in the different PSi films. The simulations modeled the experimental shift in reflectance measurements after QD attachment and the corresponding increase in EOT; with a known thickness of each film, the reflectance shift and resulting increase in EOT can be modeled accurately by changing the effective refractive index of the film. The Bruggeman effective medium approximation is then applied to estimate the effective volume fill fraction of QDs necessary to

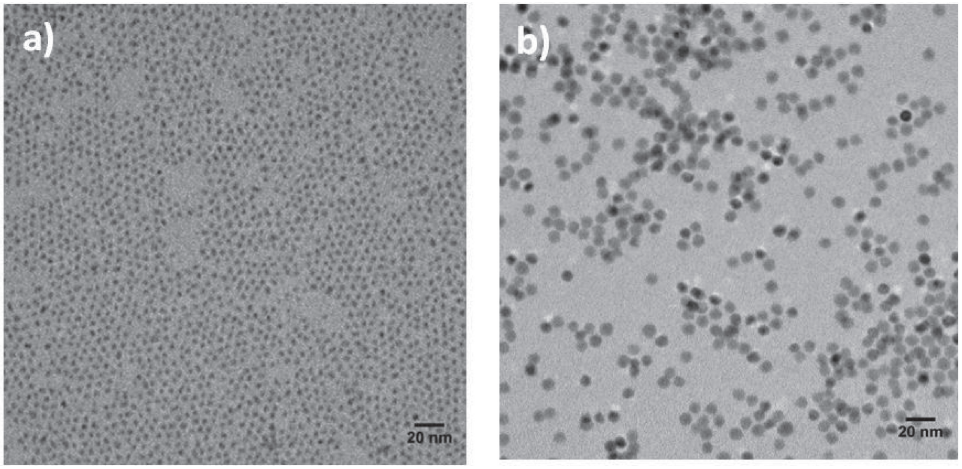

Figure 5. HR-TEM microscopy images of a) 2.8 nm and b) 7.5 nm PbS QDs.

Table 3. Quantification of small (2.8 nm) and large (7.5 nm) PbS QDs coupled with PSi films of different pore sizes based on estimated refractive index increases of the PSi films.

Average pore size [nm]	Estimated increase in effective refractive index of PSi with QD coupling		Estimated surface density (SD) [m^{-2}] and percent total surface area (% SA) coverage of QDs coupled with PSi			
	Small QDs	Large QDs	Small QDs		Large QDs	
			SD	% SA	SD	% SA
12	0.0260	0.030	1.05×10^{15}	2.05	4.37×10^{14}	2.24
15	0.0425	0.053	1.35×10^{15}	5.35	1.1×10^{15}	3.50
20	0.0460	0.057	2.26×10^{15}	10.68	1.42×10^{15}	7.14
25	0.0470	0.073	2.54×10^{15}	13.40	2.32×10^{15}	11.65
30	0.0340	0.030	1.85×10^{15}	10.72	1.32×10^{15}	5.67

achieve the simulated change in effective refractive index by taking into account the size of the QDs, the effective refractive index of the surface functionalized PSi, and the refractive index of the QDs. Note that the refractive index of the QD layer was taken to be the bulk refractive index of PbS (n = 4.15), which likely results in a slight overestimation of the refractive index for the QDs and a slight underestimation in the volume fill fraction of the QDs.[49] From the volume fill fraction of QDs, the number of coupled QDs on the pore walls can be estimated and, taking into account the total specific surface area for binding events to take place from Figure 2, QD densities on the pore walls and their percent surface area coverages can be estimated. **Table 3** summarizes the results for the ten PSi samples, showing QD densities and percent surface area coverages. High surface densities of approximately 10^{15} m^{-2} are achieved in the surface functionalized PSi. The surface area coverage of the QDs is slightly smaller but in the same range as that reported for DNA molecules in PSi waveguides with comparable pore sizes.[50] In order to more easily understand the trends presented in Table 3, we plot the relative change in optical thickness of the different thickness PSi films upon infiltration of the small and large QDs in **Figure 6**, which mirrors the trends of the surface density and percent surface area coverage in Table 3.

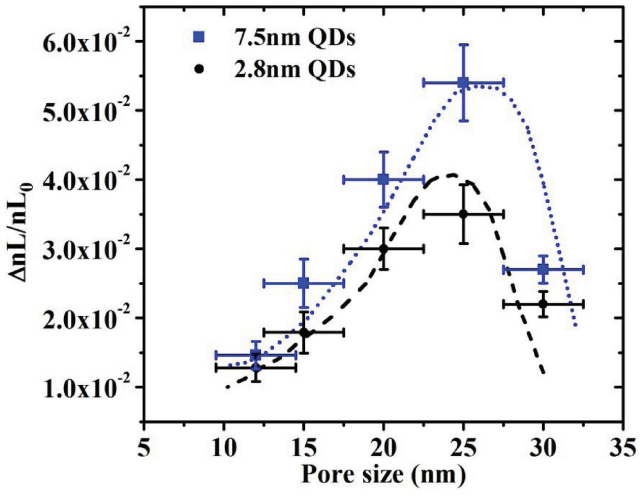

Figure 6. Relative increase in optical thickness of ≈5.5 µm PSi layers with varying average pore size after immobilizing two different sized QDs (2.8 nm and 7.5 nm). Each data point represents the average value based on three sets of experiments and the dotted and dashed lines serve as guides to the eye.

There is a clear dependence of QD binding on PSi pore size, as well as QD size, which suggests that parameters of PSi films for sensing applications must be tuned carefully to enable maximum binding of desired molecules. As shown in Figure 6, the highest relative increase in optical thickness ($\Delta nL/nL_0$) after QD attachment occurs for PSi with ≈25 nm pores, which suggests that the 25 nm pore films will give the largest response for the capture of molecules with sizes ranging from at least 2.8 nm to 7.5 nm. For larger QDs, we expect the peak value of $\Delta nL/nL_0$ to occur for samples with larger pores. The shape of the trend lines in Figure 6 suggest that the value of $\Delta nL/nL_0$ for a PSi film initially increases with pore size because the QDs can more easily infiltrate into the pores. Beyond the optimum pore size to QD size ratio, the reduced surface area available for binding events to take place dominates the ease of infiltration of QDs, fewer QDs bind within the porous matrix, and the effective refractive index increase for the films is reduced thereby resulting in a decrease in the value of $\Delta nL/nL_0$. Despite the slightly lower surface area coverage of the 7.5 nm QDs as compared to the 2.8 nm QDs, the increase in effective refractive index and the values of $\Delta nL/nL_0$ are greater than that achieved with coupling smaller QDs to PSi due to their larger diameter, which results in a significantly higher increase in the net refractive index change upon coupling with PSi. We note that for the PSi sample with an average pore size of ≈12 nm, the small increase in optical thickness due to the large QDs can be entirely attributed to the infiltration and coupling of these QDs with pore sizes exceeding ≈20 nm, which comprise ≈25% of the available surface area in the PSi sample (see Figure 1). The morphology of the pores also appear to play an important role in this size relationship. Based on cross-sectional SEM analysis of the pore structure formed at different etching current densities (Supporting Information Figure S1), for etching current densities greater than 20 mA cm^{-2} (Table 1), the rough dendritic structure of the pores changes to a smoother more cylindrical shape, aiding the infiltration of species into the nanoporous layer and thereby improving the signal response observed for QD attachment. Overall, the results shown in Figure 6 suggest that pores need to be at least three times larger than the size of nominally spherical target species to allow for diffusion and coupling within the nanoporous framework.

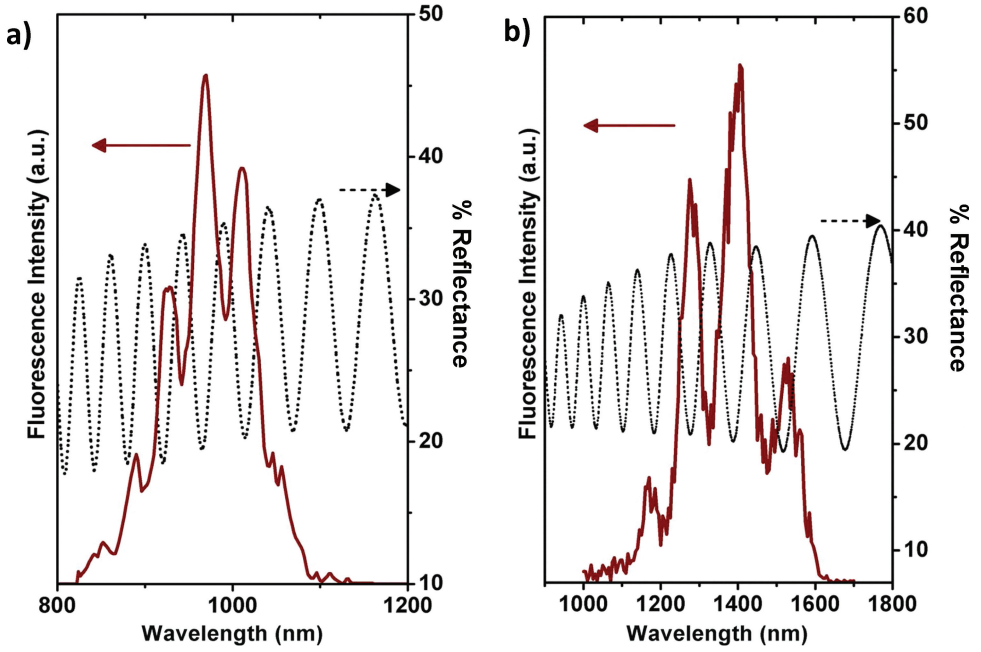

Figure 7. QD fluorescence spectra from PSi films (5.5 µm thick, 25 nm average pore diameter) infiltrated with a) small (2.8 nm) PbS QDs or b) large (7.5 nm) PbS QDs. The QD emission occurs in the expected wavelength regions based on the size of the QD. The modulated fluorescence (solid line) is due to thin film interference phenomena that also appear in the overlayed reflectance spectra (dotted line).

4.2.1. Measurement of Fluorescence Spectra from QDs coupled with PSi

In addition to the increase in effective refractive index of the PSi layer and measurable shift in the reflectance spectra upon QD attachment in the pores, observation of QD fluorescence modulated by the PSi film serves as a secondary small molecule detection mode confirming QD infiltration and coupling with PSi. **Figure 7** shows the measured fluorescence and overlaid reflectance spectra after coupling small and large PbS QDs with PSi films having ≈25 nm pores. The QD fluorescence after immobilization in PSi correlates to that measured for QDs dispersed in solution phase (Supporting Information Figure S4). The interference pattern seen in the QD fluorescence profile correlates with that arising out of thin-film interference and indicates QD attachment throughout the porous matrix. We note that modulation of the fluorescence would be absent if QDs were attached only to the surface of the PSi film. We further note that dips in the reflectance pattern have a π phase shift with respect to the minima in the fluorescence pattern which is introduced in the reflectivity spectra at the air/PSi interface where $n_{air} < n_{PSi}$.

5. Specific Detection of Biotin using QD Conjugates in PSi Films

With the demonstration of effective QD infiltration in PSi and an understanding of the size relationship between QDs and PSi pores presented in Section 4, we now demonstrate the use of $AgInS_2$/ZnS (AIS/ZnS) QDs as signal amplifiers in PSi biosensors. The biotin-streptavidin system is chosen for the labeled sensing demonstration due to its strong noncovalent biological interaction.[8,11,51] Biotin molecules (≈1 nm) are conjugated to AIS/ZnS QDs (≈3 nm diameter), stabilized in aqueous phase, and specifically attached to streptavidin-functionalized PSi films which were found to exhibit excellent stability in aqueous solutions (Supporting Information Figure S5). Given the size of the additional linker molecules (≈6 nm) necessary for streptavidin-functionalization of the PSi films that reduces the size of the pore opening, PSi films with ≈30 nm pores, as-anodized, were utilized, following the analysis presented in Figure 6.

Fluorescence and reflectance measurements were performed to demonstrate and quantify the detection of QD-biotin conjugates in PSi. As shown in **Figure 8**a, modulated fluorescence is measured when the QD-biotin conjugates are captured in the streptavidin-functionalized PSi. Excellent overlap of the fluorescence spectra from QD-biotin conjugates in solution (see Supporting Information Figure S6) and when coupled with PSi is also shown, verifying that the modulated fluorescence can indeed be attributed to the AIS/ZnS QDs inside the pores. Figure 8b shows a reflectance fringe shift of ≈27 nm resulting from the attachment of QD-biotin conjugates in PSi with no anomalies seen over the entire wavelength range of 800 nm to 2000 nm (Supporting Information Figure S7). This corresponds to an increase in EOT and effective refractive index of the PSi film of ≈110 nm and ≈0.025, respectively. Control samples in which streptavidin probe molecules were not immobilized did not demonstrate any noticeable changes in reflectance (Supporting Information Figure S8) or FTIR spectra (not shown) and no QD fluorescence was visible (**Figure 9**), suggesting the absence of non-specific binding.

Using the method presented in Section 4.2 and considering the size (≈4 nm) and refractive index (≈ 2.2) of the QD-biotin

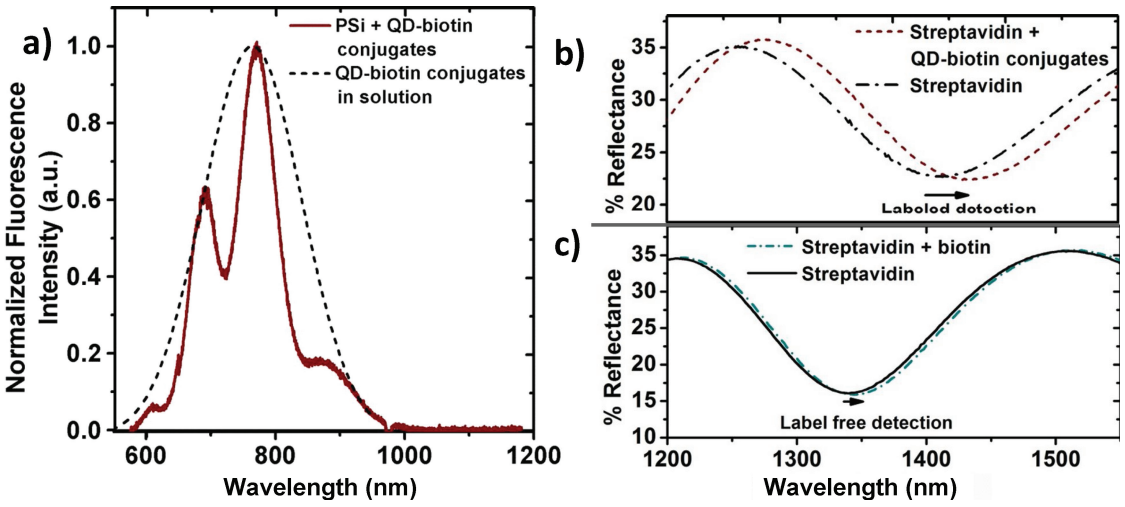

Figure 8. a) Fluorescence spectra of QD-biotin conjugates in solution and bound inside a streptavidin-functionalized PSi film. The fluorescence of the conjugates inside the PSi film is modulated due to thin film interference effects and demonstrates that the conjugates are inside as opposed to only on top of the PSi film. Reflectance spectra for the detection of biotin b) with and c) without the use of QD-conjugates from two different PSi samples functionalized with streptavidin probes. Use of the QDs conjugated to biotin molecules significantly amplifies the sensor response.

conjugates, their surface area coverage in the streptavidin-functionalized PSi is estimated to be near 6%, resulting in a surface mass density of ≈6 fg mm^{-2}. Assuming a conservative minimum resolvable reflectance fringe shift of 0.5 nm, the biotin detection limit of the QD-labeled PSi biosensor is ≈0.5 fg mm^{-2}. Hence, this sensor achieves improved sensitivity compared to unlabeled optical biosensors.[52]

We experimentally verified and quantified the signal enhancement gained through the use of the QD labels by attaching unlabeled biotin molecules to streptavidin-functionalized PSi films. As shown in Figure 8c, a reflectance fringe shift of ≈5 nm corresponding to an EOT increase of ≈10 nm results from unlabeled biotin attachment, which is in agreement with similar reports for single layer PSi biosensors[22] and is substantially less than that measured for attachment of QD-biotin conjugates. To test for non-specific binding of unlabeled biotin molecules, PSi samples, not modified by streptavidin probe molecules, were exposed to the biotin solution. The reflectance spectra did not result in any measurable change (Supporting Information Figure S9) demonstrating the absence of non-specific binding. Taking into account the size (≈1 nm), refractive index (≈1.45) and molecular weight (443.4 g mol^{-1}) for biotin, we calculate a biotin surface mass density of ≈7 pg mm^{-2} with a 1:1 binding stoichiometry with streptavidin. For a minimum resolvable fringe shift of 0.5 nm, simulations suggest a detection limit of ≈2 pg mm^{-2} for the label-free detection of biotin using PSi. Hence, QD labeling of biotin molecules amplifies the measured change in EOT by one order of magnitude and reduces the detection limit by nearly three orders of magnitude. Moreover, conjugation of biotin with QDs provides a secondary means of target molecule identification based on the distinct QD fluorescence spectrum.

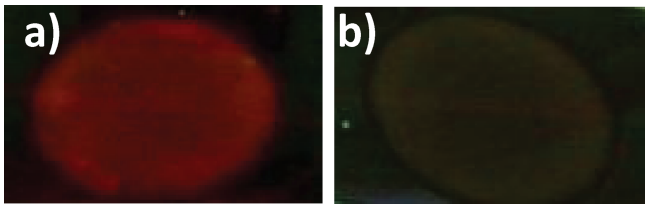

Figure 9. Images, under UV excitation at 365 nm, of a) streptavidin functionalized PSi and b) a control PSi sample (with no immobilized streptavidin probe molecules) after exposure to a QD-biotin conjugate solution and rinsing of unbound species.

6. Conclusion

Fabrication of a stable, well-characterized dual-mode QD-enhanced PSi biosensor for optical detection of small molecules has been demonstrated. Studies were performed to analyze pore size distributions, determine the available surface area for binding events to take place, and quantify the surface area coverages of QDs on the pore walls for different PSi films. The tradeoffs between ease of molecular infiltration into larger sized pores with the increase in surface area obtained with smaller sized pores were presented, and a 3:1 ratio of pore:molecule size was determined to be the minimum necessary for infiltration and attachment of spherical infiltrated species. Attachment of target QD-biotin conjugates to streptavidin molecules immobilized in the optimized PSi matrix results in a significant increase in the effective refractive index of the porous layer beyond that of unlabeled biotin immobilization and reduces the detection limit by nearly three orders of magnitude. Biotin identification is also possible by means of the secondary sensing mode whereby the conjugated QDs generate distinct fluorescence. A detection limit below 1 fg mm^{-2} was demonstrated for the labeled detection of biotin molecules using a stable streptavidin-functionalized thin film PSi sensor, which demonstrates a working range of 7 pg mm^{-2} to 0.5 fg mm^{-2}. The approach of using QD-bioconjugates coupled to PSi films opens up possibilities for biocompatible, environmentally

friendly, highly sensitive, real-time multiplexed opto-fluidic assays to study binding kinetics of analytes and detect disease markers at ultra-low concentrations without the need for complex and costly lithographic steps.

7. Experimental Section

Organic solvents used were of analytical reagent grades. The chemicals were used without further purification.

Porous Silicon Fabrication: PSi films were fabricated by electrochemical etching of boron doped p+ silicon wafers (<100>, 0.01 Ω cm, Silicon Quest) in a two-electrode configuration. A platinum wire counter-electrode and silicon wafer with an exposed area of 1.7 cm^2 were mounted on a silver plate in a Teflon etching cell. The electrolyte consisted of an ethanolic HF solution (3:8 v/v 49–51% aqueous HF:ethanol, Sigma Aldrich). Anodization was carried out in the dark. Each sample was rinsed thoroughly with ethanol and dried under a stream of nitrogen after the electrochemical etch. Tuning of the etching conditions enabled the formation of PSi films with a variety of distinct pore diameters, morphologies, and thicknesses necessary to characterize the subsequent infiltration and immobilization of nanoparticles in the porous framework. For the thickness dependent studies in Section 4.1, the following etching conditions were used. A current density of 5 mA cm^{-2} was applied for etching times of 400 s, 800 s, 1200 s, and 1600 s to form PSi films with an average pore diameter of 12 nm and thicknesses of 2 μm, 3.75 μm, 5.5 μm, and 7.25 μm, respectively. A current density of 48 mA cm^{-2} was applied for etching times of 67 s, 133 s, 200 s, and 267 s to form PSi films with an average pore diameter of 25 nm and thicknesses of 2 μm, 3.75 μm, 5.5 μm, and 7.25 μm, respectively. For the biosensing studies in Section 5, 2 μm thick PSi films with ≈30 nm average pore diameters were fabricated by applying a current density of 60 mA cm^{-2} for 66 s.

Porous Silicon Functionalization: PSi films were functionalized for two sets of experiments. The initial experiments performed with PbS quantum dots required only amine functionalization of the PSi. For these experiments, PSi samples were thermally oxidized in air at 800 °C for 30 min (Omegalux LMF-3550 Oven) forming a SiO_2 layer and characteristic Si-O-Si bonds. The samples were then rinsed with ethanol and dried under a stream of nitrogen to remove any organic surface contaminants deposited on the sample surface during oxidation. The clean oxidized PSi samples were incubated in a freshly prepared 4% 3-aminopropyltriethoxysilane (APTES) solution (50:48:4 = de-ionized water:methanol:APTES (99% Acros Organics)) for 15 min in a moist environment to provide an amine functionalized surface. The excess of unreacted APTES was thoroughly rinsed from the samples three times with ethanol and de-ionized (DI) water, dried under nitrogen flow and baked in an oven at 100 °C for 10 min to increase the cross-linking density followed by a 1 h soak in DI water to remove any unbound APTES molecules. The samples were then thoroughly rinsed with ethanol and dried under nitrogen. The 0.8 nm APTES molecules form an almost uniform monolayer over the entire PSi surface.[53] The amine-functionalized PSi films were then exposed to a 0.44 mg mL^{-1} PbS QD solution for 24 h in order to ensure saturation of all binding sites. The binding of QDs to the PSi surface was achieved through the nitrogen lone pair of the APTES amine group. This was evidenced through control experiments that exhibited no shift in reflectance spectra when PSi films unmodified by APTES were exposed to the QD solution. To ensure QDs were strongly bound to the amine ter-minated PSi surfaces, the PSi-QD films were subjected to extensive washing with anhydrous hex-ane followed by analysis of the measured reflectance spectra. The second set of experiments performed with biotin molecules and biotinylated-$AgInS_2$/ZnS QDs required additional functionalization of the PSi films. After silanization with APTES, the PSi films were exposed to the homobifuctional cross-linker glutaraldehyde.[51,54] The films were incubated in 2.5% glutaraldehyde solution, formed by mixing 50 μL of 25% aqueous glutaraldehyde (EM grade, Polysciences) with 950 μL of HEPES buffer (20 mM HEPES, 150 mM NaCl, 5 mM EDTA, pH = 7.4), for 30 min. Excess glutaraldehyde solution was removed and 1 μL of sodium cyanoborohydride (5 M cyanoborohydride, 1 M NaOH, Aldrich) in 100 μL of HEPES buffer was pipetted onto the PSi sensor in order to stabilize the Schiff base (C = N) formed during reaction of the aldehyde group with the amine group. After 30 min of incubation with the reducing agent, the PSi films were thoroughly rinsed with HEPES buffer to remove any unreacted glutaraldehyde from the nanoscale pores. Next, 100 μL of 10 μM streptavidin solution in PBS buffer was then pipetted onto the PSi sensor and incubated for 30 min. An incubation time of 30 min was found to be sufficient to ensure maximum attachment of target molecule as reported previously.[47] Thereafter, the reducing step with sodium cyanoborohydride was repeated in order to stabilize the Schiff base formed during streptavidin fixation to the pore walls. To close any unreacted aldehyde groups for minimizing non-specific binding, 3 M ethanolamine (>99% ethanolamine, Aldrich) in buffer, with pH adjusted to 9.0, was pipetted onto the PSi sensor and incubated for 30 min.[50] The PSi sample was then thoroughly rinsed with buffer and DI water and dried under air. For the labeled detection measurements, the PSi sensor was exposed to 100 μL of a 500 μM solution of QD-biotin conjugates and incubated for 30 min. The sample was then thoroughly rinsed with buffer and DI water, and then dried under air. Control experiments were performed to ensure that no QD-biotin conjugates would attach to surface functionalized PSi sensors that had no streptavidin probe molecules. The aldehyde functionalized PSi sensors were also exposed to 100 μL of a 500 μM solution of QD-biotin conjugates and incubated for 30 min. These samples were rinsed with buffer and DI water, and dried under air. For label-free detection, 100 μL of 200 μM sulfo-NHS-biotin (Sigma Aldrich) solution in HEPES buffer was pipetted onto a streptavidin (Sigma Aldrich) functionalized PSi sensor. This high concentration ensured that all accessible streptavidin binding sites were saturated with biotin molecules as lower concentration solutions of 100 μM and 150 μM also produced the same magnitude of reflectance fringe shift that resulted in ≈10 nm increase in EOT of the PSi film and a surface mass density of ≈7 pg mm^{-2}. Following incubation of the sample in the biotin solution for 30 min, the sample was rinsed with buffer and DI water, and then dried under air. In control experiments for the unlabeled detection of biotin molecules, 100 μL of 200 μM sulfo-NHS-biotin solution in HEPES buffer was pipetted onto PSi sensors that had no streptavidin probe molecules and incubated in the biotin solution for 30 min. The samples were rinsed with buffer and DI water, and dried under air.

SEM Image Analysis: Thresholding of the gray-scale top-view SEM images of PSi in Matlab yields binary images that allow for straightforward differentiation between the pores and the silicon pore wall framework. After noise removal using mathematical morphological openings and closings on the thresholded image,[55] pore areas in pixel count were extracted using the function regionprops in Matlab. The pore areas were then expressed in nm^2 by application of a conversion factor based on the ratio of the SEM scale bar pixel count to the corresponding length in nm. All pores were approximated to cylinders and the effective pore diameters were calculated from the extracted pore areas.

Nitrogen Adsorption Measurements: In order to achieve isotherms for Brunauer, Emmett, and Teller theory analysis, 20 μm thick porous samples were degassed at 200 °C temperatures for 16 h. Adsorption isotherms were measured using a Micromeritics ASAP 2020 at 77 K and surface area estimates were made using a reported procedure.[56]

Synthesis of PbS Quantum Dots: PbS QDs were prepared using a reported procedure.[57,58] The QDs synthesis was carried out inside a glove box under nitrogen atmosphere. Briefly, 2 mmol of lead (II) oxide (PbO, 99.99%, Acros Organics), 2.7 mmol of oleic acid (OA, Aldrich) and 4 mL of octadecene (ODE, Lancaster) were mixed in a 25 ml three neck flask under a magnetic stirring. After degassing and purging by argon at 80 °C, the mixture was subsequently heated to 140 °C. After complete dissolution of PbO, the solution was cooled to 120 °C and 2 mL of ODE with bis(trimethylsilyl)sulfide (1 mmol, 98%, Alfa Aesar) was rapidly injected into the solution under constant stirring. After the temperature decreased to 110 °C, resulting from the injection of the precursor, an additional 2 mL of ODE was added into the solution. Growth of the QDs was carried out at 100 °C for 30 s. Synthesized QDs were then

removed from the reaction vessel with a glass syringe. The resulting PbS QDs were purified twice by acetone precipitation from chlorofom solution and centrifugation to remove unreacted precursors. Finally, the desired PbS QDs were redissolved in hexane, yielding an optically clear brown solution. By controlling chemical synthesis conditions and the concentration of precursors, different sizes (2.8 nm and 7.5 nm) of PbS QDs were prepared.

Synthesis and Functionalization of $AgInS_2$/ZnS (AIS/ZnS) Quantum Dots: $AgInS_2$/ZnS QDs were synthesized by a procedure published elsewhere.[59,60] The single source precursor $(AgIn)(S_2CN(C_2H_5)_2)_4$ was prepared directly through the precipitation of stoichiometric amounts of indium acetate ($In(CH_3COO)_3$, 99%, Alfa Aesar), silver nitrate ($AgNO_3$, 99.8%, Aldrich) and sodium diethyldithiocarbamate ($NaS_2CN(C_2H_5)_2S{\cdot}3H_2O$, 98%, Alfa Aesar) in DI water. $Zn(S_2CN(C_2H_5)_2)_2$ was prepared in the same manner using zinc acetate ($Zn(CH_3COO)_2$, 99.98%, Alfa Aesar). Both precursors were thoroughly washed by water and dried in a vacuum before further use.

In the synthesis of $AgInS_2$ (AIS) QDs, a previously degassed mixture of 50 mg of precursor and 3 mL of oleylamine (OLA, Aldrich) was heated to 180 °C under a stream of Ar and constant magnetic stirring. After allowing QDs to grow for 8 min, the brown solution was removed by a syringe. After being cooled to room temperature, the QD solution was separated from large agglomerates by centrifugation at 4500 rpm for 10 min. AIS QDs were then washed from unreacted precursor by precipitating with 10 mL of acetone and isolated by centrifugation and decantation. To grow the ZnS shell, the AIS QDs and 10 mg of $Zn(S_2CN(C_2H_5)_2)_2$ were redissolved in 3 mL of OLA. The mixture was degassed and subsequently heated to 180 °C for 20 min. The prepared AIS/ZnS QDs were subjected to a washing procedure as described for AIS QDs. Finally AIS/ZnS QDs were dissolved in 1 mL of chloroform.

Water solubilization of AIS/ZnS QDs was achieved using a ligand exchange strategy described in ref. [61–63] Typically, 1 mL of glutathione (GSH, 30 mg, 98%, Acros Organics) methanolic solution with pH adjusted to 12 by tetramethylammonium hydroxide (TMAH, 25% solution in methanol, Acros Organics) was added dropwise to a chloroform solution of QDs (30 µmol) under constant stirring. The solution was left while stirring for 24 h. Then, 1 mL of water was added and the mixture was kept stirring for another hour. After being transferred into upper aqueous phase, the QDs were isolated and washed with acetone several times before finally being dispersed in water. GSH functionalized QDs were washed from excess ligands using a Microcon Centrifugal Unit (Ultracel YM-10, MWCO = 10,000).

AIS/ZnS QDs were conjugated to biotin according to the following protocol.[64] 1 µmol of GSH coated AIS/ZnS QDs were incubated with 0.5 mg of sulfo-NHS-biotin in PBS buffer for 30 min at room temperature. After incubation, biotin conjugated QDs were washed from the excess of unreacted sulfo-NHS-biotin using the Ultracel YM-10.

Interferometric Reflectance Measurements: Reflectance spectra were measured at room temperature with a Varian Cary 5000 UV-VIS-NIR spectrophotometer at a step size of 0.5 nm. Reflectance spectra were collected over a wavelength range of 500 nm to 2000 nm over a spot size of ≈6 mm in diameter at the center of the PSi sample.

Transmission Electron Microscopy (TEM): HRTEM analysis was performed using a Philips CM20 TEM operating at 200 kV. The samples for TEM investigation were prepared by dropping a solution of washed QDs onto carbon coated copper grids.

Scanning Electron Microscopy (SEM): Pore size and morphology were studied using a Hitachi S-4200 scanning electron microscope. Samples were mounted on the sample holder using carbon tape. An accelerating voltage of 10 kV was used during sample imaging.

IR QD Fluorescence Measurements: A Coherent Innova 70C water-cooled argon–krypton laser operating at a wavelength of 488 nm and ≈10 mW cm^{-2} optical power was used to excite fluorescence from PSi samples over a spot size of 0.8 cm^2. The beam was chopped at 40 Hz by a Stanford Research Systems model SR540 chopper controller. A thermoelectrically cooled InGaAs Oriel detector (model 71646) and a Stanford Research Systems model SR830 lock-in amplifier were used to measure the fluorescence intensity at the output port of a 74100 Oriel Cornerstone 260 ¼ m monochromator, fitted with a 600 line mm^{-1} grating blazed at 1250 nm, over a wavelength range of 800 nm–1650 nm through a 2×7 mm^2 slit.

Visible QD Fluorescence Measurements: A fiber-coupled Ocean Optics USB4000 CCD spectrometer was used to record visible QD emission between 500 nm and 1000 nm.

FTIR Characterization: Measurements were conducted using a Tensor 27 FTIR spectrometer (Bruker Optics Inc.) equipped with the Seagull variable angle reflection accessory (Harrick Scientific Products Inc.) for specular reflectance measurements from solid surfaces and Opus 5.5 software. FTIR spectra were collected in 84 scans at a 4 cm^{-1} resolution in a nitrogen purged compartment.

Supporting Information

Supporting Information is available from the Wiley Online Library or from the author.

Acknowledgements

This work was funded in part by the Army Research Office (Grant no. W911NF-08-1-0200 and W911NF-09-1-0101) and by the Defense Threat Reduction Agency (Grant no. HDTRA1-10-1-0041). Electron microscopy imaging, FTIR spectroscopy, and spectrophotometry measurements were performed in the Vanderbilt Institute of Nanoscale Science and Engineering, using facilities renovated under NSF ARI-R2 DMR-0963361. The authors thank Prof. M. Douglas LeVan and Amanda Furtado for help with the nitrogen adsorption measurements. The authors gratefully acknowledge Benjamin Lawrie, Jenifer Lawrie, Judson Ryckman and Aminah Hamzah for useful technical discussions.

Received: September 17, 2012
Revised: December 14, 2012
Published online: February 27, 2013

[1] B. Dubertret, P. Skourides, D. J. Norris, V. Noireaux, A. H. Brivanlou, A. Libchaber, *Science* **2002**, *298*, 1759.
[2] M. Howarth, K. Takao, Y. Hayashi, A. Y. Ting, *Proc. Natl. Acad. Sci. USA* **2005**, *102*, 7583.
[3] G. Rousserie, A. Sukhanova, K. Even-Desrumeaux, F. Fleury, P. Chames, D. Baty, V. Oleinikov, M. Pluot, J. H. M. Cohen, I. Nabiev, *Crit. Rev. Oncol. Hematol.* **2010**, *74*, 1.
[4] M. Suzuki, Y. Husimi, H. Komatsu, K. Suzuki, K. T. Douglas, *J. Am. Chem. Soc.* **2008**, *130*, 5720.
[5] I. L. Medintz, H. Mattoussi, A. R. Clapp, *Int. J. Nanomed.* **2008**, *3*, 151.
[6] K. Sapsford, T. Pons, I. Medintz, H. Mattoussi, *Sensors* **2006**, *6*, 925.
[7] X. Michalet, F. F. Pinaud, L. A. Bentolila, J. M. Tsay, S. Doose, J. J. Li, G. Sundaresan, A. M. Wu, S. S. Gambhir, S. Weiss, *Science* **2005**, *307*, 538.
[8] Y. Chen, H. l. Ren, N. Liu, N. Sai, X. Liu, Z. Liu, Z. Gao, B. a. Ning, *J. Agric. Food Chem.* **2010**, *58*, 8895.
[9] M. J. A. Shiddiky, S. Rauf, P. H. Kithva, M. Trau, *Biosens. Bioelectron.* **2012**, *35*, 251.
[10] Y. G. Kim, S. Moon, D. R. Kuritzkes, U. Demirci, *Biosens. Bioelectron.* **2009**, *25*, 253.
[11] K. Kerman, T. Endo, M. Tsukamoto, M. Chikae, Y. Takamura, E. Tamiya, *Talanta* **2007**, *71*, 1494.
[12] J. A. Hansen, J. Wang, A.-N. Kawde, Y. Xiang, K. V. Gothelf, G. Collins, *J. Am. Chem. Soc.* **2006**, *128*, 2228.

[13] I. L. Medintz, A. R. Clapp, J. S. Melinger, J. R. Deschamps, H. Mattoussi, *Adv. Mater.* **2005**, *17*, 2450.
[14] W. C. W. Chan, S. Nie, *Science* **1998**, *281*, 2016.
[15] B. Sun, W. Xie, G. Yi, D. Chen, Y. Zhou, J. Cheng, *J. Immunol. Methods* **2001**, *249*, 85.
[16] E. Goldman, I. Medintz, H. Mattoussi, *Anal. Bioanal. Chem.* **2006**, *384*, 560.
[17] I. L. Medintz, H. T. Uyeda, E. R. Goldman, H. Mattoussi, *Nat. Mater.* **2005**, *4*, 435.
[18] B. Schuler, W. A. Eaton, *Curr. Opin. Struct. Biol.* **2008**, *18*, 16.
[19] K. A. Merchant, R. B. Best, J. M. Louis, I. V. Gopich, W. A. Eaton, *Proc. Natl. Acad. Sci. USA* **2007**, *104*, 1528.
[20] C. Pacholski, M. Sartor, M. J. Sailor, F. Cunin, G. M. Miskelly, *J. Am. Chem. Soc.* **2005**, *127*, 11636.
[21] A. Janshoff, K. P. S. Dancil, C. Steinem, D. P. Greiner, V. S. Y. Lin, C. Gurtner, K. Motesharei, M. J. Sailor, M. R. Ghadiri, *J. Am. Chem. Soc.* **1998**, *120*, 12108.
[22] J. M. Buriak, M. P. Stewart, T. W. Geders, M. J. Allen, H. C. Choi, J. Smith, D. Raftery, L. T. Canham, *J. Am. Chem. Soc.* **1999**, *121*, 11491.
[23] B. E. Collins, K. P. S. Dancil, G. Abbi, M. J. Sailor, *Adv. Funct. Mater.* **2002**, *12*, 187.
[24] J. L. Lawrie, J. Yang, S. M. Weiss, *Nano. IEEE Trans.* **2010**, *9*, 596.
[25] M. P. Stewart, J. M. Buriak, *Adv. Mater.* **2000**, *12*, 859.
[26] Y. Jiao, D. S. Koktysh, N. Phambu, S. M. Weiss, *Appl. Phys. Lett.* **2010**, *97*, 153125.
[27] G. Rong, J. Ryckman, R. Mernaugh, S. M. Weiss, *Appl. Phys. Lett.* **2008**, *93*, 161109.
[28] S. Gold, K.-L. Chu, C. Lu, M. A. Shannon, R. I. Masel, *J. Power Sources* **2004**, *135*, 198.
[29] T. Pichonat, B. Gauthier-Manuel, D. Hauden, *Fuel Cells Bull.* **2004**, *2004*, 11.
[30] S. Aravamudhan, A. R. A. Rahman, S. Bhansali, *Sens. Actuators A* **2005**, *123-124*, 497.
[31] R. R. Bilyalov, R. Lüdemann, W. Wettling, L. Stalmans, J. Poortmans, J. Nijs, L. Schirone, G. Sotgiu, S. Strehlke, C. Lévy-Clément, *Sol. Energy Mater. Sol. Cells* **2000**, *60*, 391.
[32] P. Menna, G. Di Francia, V. La Ferrara, *Sol. Energy Mater. Sol. Cells* **1995**, *37*, 13.
[33] S. Yae, Y. Kawamoto, H. Tanaka, N. Fukumuro, H. Matsuda, *Electrochem. Commun.* **2003**, *5*, 632.
[34] E. Gultepe, D. Nagesha, S. Sridhar, M. Amiji, *Adv. Drug Delivery Rev.* **2010**, *62*, 305.
[35] J. Salonen, L. Laitinen, A. M. Kaukonen, J. Tuura, M. Björkqvist, T. Heikkilä, K. Vähä-Heikkilä, J. Hirvonen, V. P. Lehto, *J. Controlled Release* **2005**, *108*, 362.
[36] E. J. Anglin, L. Cheng, W. R. Freeman, M. J. Sailor, *Adv. Drug Delivery Rev.* **2008**, *60*, 1266.
[37] J. Salonen, A. M. Kaukonen, J. Hirvonen, V.-P. Lehto, *J. Pharm. Sci.* **2008**, *97*, 632.
[38] E. C. Wu, J. H. Park, J. Park, E. Segal, F. D. Cunin, M. J. Sailor, *ACS Nano* **2008**, *2*, 2401.
[39] J. H. Park, L. Gu, G. von Maltzahn, E. Ruoslahti, S. N. Bhatia, M. J. Sailor, *Nat. Mater.* **2009**, *8*, 331.
[40] E. Tasciotti, X. Liu, R. Bhavane, K. Plant, A. D. Leonard, B. K. Price, M. M.-C. Cheng, P. Decuzzi, J. M. Tour, F. Robertson, M. Ferrari, *Nat. Nanotechnol.* **2008**, *3*, 151.
[41] C. Chiappini, E. Tasciotti, J. R. Fakhoury, D. Fine, L. Pullan, Y. C. Wang, L. Fu, X. Liu, M. Ferrari, *ChemPhysChem.* **2010**, *11*, 1029.
[42] J. Qian, C. Zhang, X. Cao, S. Liu, *Anal. Chem.* **2010**, *82*, 6422.
[43] R. Herino, G. Bomchil, K. Barla, C. Bertrand, J. L. Ginoux, *J. Electrochem. Soc.* **1987**, *134*, 1994.
[44] X. G. Zhang, *J. Electrochem. Soc.* **2004**, *151*, C69.
[45] V. K. S. Hsiao, J. R. Waldeisen, Y. Zheng, P. F. Lloyd, T. J. Bunning, T. J. Huang, *J. Mater. Chem.* **2007**, *17*, 4896.
[46] L. Dyadyusha, H. Yin, S. Jaiswal, T. Brown, J. J. Baumberg, F. P. Booy, T. Melvin, *Chem. Commun.* **2005**, *25*, 3201.
[47] G. Gaur, D. Koktysh, S. M. Weiss, *Mater. Res. Soc. Symp. Proc.* **2011**, *1301*, 241.
[48] P. Yeh, *Optical Waves in Layered Media*, John Wiley & Sons, Inc., Hoboken **1988**.
[49] R. R. Reddy, Y. Nazeer Ahammed, K. Rama Gopal, P. Abdul Azeem, B. Sasikala Devi, T. V. R. Rao, S. H. Behere, *Opt. Mater.* **2003**, *22*, 7.
[50] G. Rong, A. Najmaie, J. E. Sipe, S. M. Weiss, *Biosens. Bioelectron.* **2008**, *23*, 1572.
[51] H. Lu, G. Yi, S. Zhao, D. Chen, L. H. Guo, J. Cheng, *J. Mater. Chem.* **2004**, *14*, 1336.
[52] X. Fan, I. M. White, S. I. Shopova, H. Zhu, J. D. Suter, Y. Sun, *Anal. Chim. Acta.* **2008**, *620*, 8.
[53] H. Ouyang, C. C. Striemer, P. M. Fauchet, *Appl. Phys. Lett.* **2006**, *88*, 163108.
[54] S. T. Kim, D. J. Kim, T. J. Kim, D. W. Seo, T. H. Kim, S. Y. Lee, K. Kim, K. M. Lee, S. K. Lee, *Nano. Lett.* **2010**, *10*, 2877.
[55] P. Maragos, R. W. Schafer, *Proc. IEEE* **1990**, *78*, 690.
[56] K. Sing, *Colloids Surf., A* **2001**, *187-188*, 3.
[57] M. A. Hines, G. D. Scholes, *Adv. Mater.* **2003**, *15*, 1844.
[58] D. S. Koktysh, J. R. McBride, S. K. Dixit, L. C. Feldman, S. J. Rosenthal, *Nanotechnology* **2007**, *18*, 495607.
[59] T. Torimoto, T. Adachi, K. Okazaki, M. Sakuraoka, T. Shibayama, B. Ohtani, A. Kudo, S. Kuwabata, *J. Am. Chem. Soc.* **2007**, *129*, 12388.
[60] T. Torimoto, S. Ogawa, T. Adachi, T. Kameyama, K. I. Okazaki, T. Shibayama, A. Kudo, S. Kuwabata, *Chem. Commun.* **2010**, *46*, 2082.
[61] B. K. Pong, B. L. Trout, J. Y. Lee, *Langmuir* **2008**, *24*, 5270.
[62] X. H. Zhong, W. J. Zhang, G. J. Chen, J. Wang, B. C. Ye, *Inorg. Chem.* **2009**, *48*, 9723.
[63] D. Koktysh, V. Bright, W. Pham, *Nanotechnology* **2011**, *22*, 275606.
[64] Y. G. Zheng, S. J. Gao, J. Y. Ying, *Adv. Mater.* **2007**, *19*, 376.